Silicon
https://doi.org/10.1007/s12633-023-02383-w

ORIGINAL PAPER

Surface Modified Silicon Dioxide Based Functional Adsorbents Derived From Waste Sand for the Removal of Toxic Pollutants From Water

Harshada B. Garud[1] · Sushilkumar A. Jadhav[2] · Sayali P. Jadhav[2] · Pradnya S. Suryawanshi[2] · Vilas A. Kalantre[1] · Shivaji H. Burungale[3] · Sagar D. Delekar[4] · Pramod S. Patil[2,5]

Received: 29 December 2022 / Accepted: 28 February 2023

Abstract

Waste foundry sand (WFS), an industrial waste mainly comprising silicon dioxide was used to generate low-cost and efficient adsorbents for the expulsion of toxic pollutants from water through adsorption. The WFS was converted into particles by top–down approach followed by subsequent activation and functionalization. Activated sand particles (ASPs) with –OH groups and amino-functionalized sand particles (AFSPs) with $–NH_2$ groups were synthesized and fully characterized using FESEM, EDX, ATR-FTIR, XRD, TGA, and BET analyses. The adsorption capacities at experimental conditions for cationic dyes namely methylene blue(MB), malachite green(MG), methyl violet (MV), rhodamine B(Rh B) were 38.16, 26.31, 55.24 and 35.84 mg g^{-1} while for anionic dyes namely methyl orange (MO), patent blue VF(PB VF), quinoline yellow(QY), reactive Red 2(RR 2) were 7.28, 4.63, 7.84 and 6.91 mg g^{-1} as well as for metal ions namely Cd(II)), Ni(II)), Co(II)), and Cr(VI)were 23.81, 43.06, 17.03 and 3.47 mg g^{-1} respectively. The adsorption equilibrium isotherms optimally fit the Langmuir isotherm model, indicating homogeneous surfaces and monolayer adsorption. A pseudo-second-order model showed a strong agreement with the experimental data, thus identifying chemisorption as the rate-limiting step. Additionally, these particles were verified to be reusable for a minimum five adsorption–desorption cycles without loss of efficiency.

Keywords Waste foundry sand · Dyes · Heavy metal ions · Adsorption · Pollutant removal

1 Introduction

Metal casting foundry industries produce waste foundry sand (WFS) as a solid waste material. WFS is classified as a hazardous waste material that may cause critical health problems [1, 2]. Massive growth of the foundry industry makes it an alarming issue at the global level. Industries choose the most straightforward approach to tackle these potential problems by reducing waste sand and recovery at the source [3]. However, WFS cannot be completely nullified. The conversion of WFS into value-added products and its recycling can be important strategies to tackle the problem. The benefits of such approaches will save natural resources, energy and environment [4].

Water contamination has emerged as one of the critical global challenges in the twenty-first century [5, 6]. For removing contaminants from potable water, several techniques have been developed, namely, adsorption [7–12], flocculation [13], coagulation [14, 15], electrolysis [16],

✉ Sushilkumar A. Jadhav
sushil.unige@gmail.com

✉ Shivaji H. Burungale
shivajiburungale777@gmail.com

✉ Pramod S. Patil
psp_phy@unishivaji.ac.in

[1] Balasaheb Desai College, Patan, affiliated to Shivaji University Kolhapur, Vidyanagar, Kolhapur 416004, Maharashtra, India

[2] School of Nanoscience and Technology, Shivaji University Kolhapur, Vidyanagar, Kolhapur 416004, Maharashtra, India

[3] Yashwantrao Chavan College of Science, Karad, affiliated to Shivaji University Kolhapur, Vidyanagar, 416004 Kolhapur, Maharashtra, India

[4] Department of Chemistry, Shivaji University Kolhapur, Vidyanagar, 416004 Kolhapur, Maharashtra, India

[5] Department of Physics, Shivaji University Kolhapur, Vidyanagar, 416004 Kolhapur, Maharashtra, India

Published online: 07 March 2023

biodegradation [17, 18] and photocatalytic degradation [19–23]. However, each of these processes has its flaws and limitations such as inefficient operation, toxic waste formation, the requirement for specific chemicals, large amounts of sludge production and excessive energy usage. Adsorption is a physicochemical interaction where atoms, ions or molecules get adsorbed or connected on the outer layer of the solid surface. The removal of pollutants via adsorption is preferred owing to its simplicity, operational ease, cost effectiveness [24] and no secondary pollution. Adsorbent materials can be easily regenerated [25], are not affected by toxic pollutants and they enable fast operating speeds [26], smooth operations and high efficiency [27]. Furthermore, no intermediate by-products are produced during adsorption, which reduces the chances of secondary pollution [28]. Adsorption is thus widely used for industrial effluent treatment [29]. Several industrial effluents contain dyes for example, those from textile, paper, rubber, plastics, paints, printing or leather industries [30–33]. Metallurgical and metal plating industries lead to heavy metal pollution [34, 35]. Many industries such as electroplating, textile, tanning and batteries discard their wastewater directly in fresh aqueous streams [36]. Adsorption removal of pollutants by using efficient and low cost adsorbents will benefit effluent treatment processes in such industries.

In this study, WFS-derived adsorbent materials were developed via size reduction using the top–down approach to obtain the particles followed by their activation and chemical functionalization with suitable groups. The adsorbent materials were successfully used to remove cationic and anionic dyes as well as toxic heavy metal ions from water. The significant features of the work are exclusion of the pH adjustment procedure in the adsorption removal of pollutants, the capability of adsorption of both organic and inorganic pollutants by the developed adsorbents and importantly the possibility of the recovery of the adsorbed dyes. The results demonstrate the adsorption removal capacity, reusability and chemical stability of the adsorbent material for several model pollutants used in the study. The adsorbents can be reused after several cycles without considerable loss in adsorption capacity. The findings of this study provide important insights for developing low- or no-cost advanced materials for water purification. The complete experimental design covering wide range of pollutants and development of a functional material based adsorbent. This work signifies the possibility for recovery of different dyes and advancement in the field of development of highly efficient yet low cost adsorbents for water purification technology. This approach also provide an alternative solution to the alarming waste sand disposal issue faced by the foundries worldwide.

2 Experimental

2.1 Chemicals and Materials

Sodium hydroxide (NaOH, 99%) and 3-aminopropyltrieth-oxysilane (APTES, 99%, Sigma-Aldrich) were used for the activation and functionalization of sand particles, respectively. The cationic dyes used were methylene blue (MB, $C_{16}H_{18}ClN_3S$, Thermo Fisher Scientific India Pvt., Ltd.), malachite green (MG, $C_{23}H_{25}ClN_2$, Basic Green 4, Certified, C.N. DcMg-11), methyl violet (MV, $C_{25}H_{30}ClN_3$, Poona Chemical Laboratory), and rhodamine B (Rh B, $C_{28}H_{31}ClN_2O_3$, Molychem India Pvt., Ltd.). The anionic dyes used were methyl orange (MO, $C_{14}H_{14}N_3NaO_3S$, Loba Chemie Pvt., Ltd.), patent blue VF (PB VF, $C_{54}H_{62}CaN_4O_{14}S_4$, Sigma-Aldrich), quinoline yellow (QY, $C_{18}H_{13}NO_5/_8/_{11}S_1/_2/_3Na_1/_2/_3$, Sigma-Aldrich), and reactive Red 2 (RR 2, $C_{19}H_9Cl_2N_6Na_3O_{10}S_3$, Sigma-Aldrich). Heavy metal ions sources included cadmium sulfate ($3CdSO_4.8H_2O$, s.d. fine-Chem Ltd., Mumbai), nickel sulfate ($NiSO_4.6H_2O$, Thomas Baker Pvt., Ltd.), cobalt nitrate ($Co(NO_3)_2\ 6H_2O$, 99%, Thomas Baker Pvt., Ltd.), and potassium dichromate ($K_2Cr_2O_7$, 99.5%, Loba Chemie Pvt., Ltd.). All chemicals used were analytical grade reagents. Ethanol was used for the desorption experiments. All solutions were prepared in deionized water.

2.2 Instruments and Methods

Field emission scanning electron microscopy (FESEM, Tescan, Micra3) was used to study the morphology of sand-based composite particles. Functional group detection was performed using Attenuated Total Reflection Fourier-transform infrared spectroscopy (ATR-FTIR, Lambda, Australia) by using sample (10 wt.%) pressed into KBr pellets. Advanced ATR-FTIR baseline correction was applied to all spectra in the range of 4000–500 cm^{-1}. The Brunauer–Emmett–Teller (BET, Quantachrome NOVA 1000e, USA) instrument was used to investigate the surface area and pore size distribution of the samples. The crystal structures and phases of sand particles were studied using X-ray diffraction (XRD, Brucker, D2 Phased diffractometer) using CuKα radiation with wavelength of 1.5406 Å. Thermo gravimetric analyses (TGA) were carried out on a Q500 model from TA instrument by heating samples at a rate of 10 °C/min up to 900 °C under a nitrogen flow and from 25 to 800 °C in an air atmosphere. The concentrations of the dyes were determined by using a PC-based double beam spectrophotometer (2202–SYSTRONICS); the readings were taken at 25 to 30 °C. The concentrations of the metal ions were determined by using an atomic absorption spectrophotometer (AAS, AA S-263–SYSTRONICS) at room temperature.

2.3 Methods for Activation and Functionalization of Sand Particles

2.3.1 Sand Collection and Pre-treatment

WFS samples were collected from various sites. The metal impurities in these samples were removed by using a strong magnet and then the samples were washed 4 to 5 times with double distilled water to remove water-soluble and floating impurities.

2.3.2 Size Reduction By Ball Milling

The washed WFS samples were subjected to ball milling under specific optimized conditions with 12 stainless steel balls at approximately 450–500 rpm for 30 min. The ball-milled sand was washed 7 to 8 times with double distilled water to remove any remaining coal or other impurities. After washing, the samples were dried in oven at 70 °C overnight.

2.3.3 Synthesis of Activated Sand Particles (ASPs)

The ball-milled and washed sand particles were activated by treatment with a strong base. The particles were dispersed in 100 mL of a 1 M aqueous solution of NaOH. The dispersions were stirred continuously using a magnetic stirrer at 60–70 °C for approximately 12 h. ASPs were recovered by centrifugation at 5000 rpm and then washed 4 to 5 times with double distilled water and dried in the oven for 24 h at 100 °C [37].

2.3.4 Synthesis of Amino Functionalized Sand Particles (AFSPs)

The ASPs were dispersed in 100 mL ethanol with vigorous stirring. During stirring, 2.5 mL of APTES was added to the central vortex of the solution. This suspension was stirred for 3 h at room temperature. At the end of the reaction, the stirring was stopped, and the particles were allowed to settle down. The supernatant was discarded, and the sand particles were washed 2 to 3 times with ethanol. The achieved AFSPs were dried at 70 °C for 3 h [37].

2.3.5 Dye Adsorption Experiment

The optimized adsorbent quantities of ASPs and AFSPs were added in cationic or anionic dye solutions. The suspensions were stirred using a magnetic stirrer, the centrifugation process supernatant was recovered in a cuvette by using a syringe and analyzed at 400–800 nm by UV–visible spectroscopy. The absorbance was noted after every 15 min and this procedure was carried out until maximum adsorption.

2.3.6 Dye Desorption Experiments

Dye desorption (or recovery) experiments were carried out on sand particles recovered from the dye adsorption experiments. Desorption experiments were performed by adding ethanol to the recovered ASPs and AFSPs. The suspensions were stirred using a magnetic stirrer. Supernatants were recovered after centrifugation, and their absorbance were checked to confirm the reactions of adsorbents and dye recoveries. Five successive adsorption–desorption cycles were performed on the sand particles.

2.3.7 Metal Adsorption Experiments

The optimized adsorbent quantities of AFSPs were added in Cd(II), Ni(II), Co(II), and Cr(VI) metal ion solutions. The AFSPs were kept in the solutions for approximately 3 h to ensure complete or maximum adsorption. The concentrations of Cd(II), Ni(II), Co(II), and Cr(VI) ions in the solutions before and after adsorption were monitored by AAS. The concentration was noted after every 30 min and this procedure was carried out for 180 min.

3 Results and Discussion

The waste sand particles were subjected to ball milling to obtain microparticles by top-down approach. The size reduced particles were treated with NaOH for activation and for generation of OH groups. The surface morphology of particles was changed after activation/functionalization. The activation process created large number of hydroxyl groups on the surface of particles which were used in the next step for the functionalization. The aminopropyl triethoxy silane (APTES) was used for the amino functionalization of the sand particles. The hydrolysis condensation of APTES molecule happens on the surface of sand particles and that imparts amino groups to the particles. Both these surface treated particles were fully characterized by various characterization techniques before testing them as adsorbents. The chemical structures of cationic and anionic dyes used in this study are shown in Figs. S1 and S2.

3.1 FESEM Analysis

The elemental compositions, surface textures, and morphologies of the samples were determined using FESEM. The morphologies, sizes, and compositions of particles influence the physical properties of the adsorbents. A higher surface area leads to higher available area for adsorption. The FESEM analysis revealed the morphologies and textures of the WFS (Fig. 1 A and B), ASPs

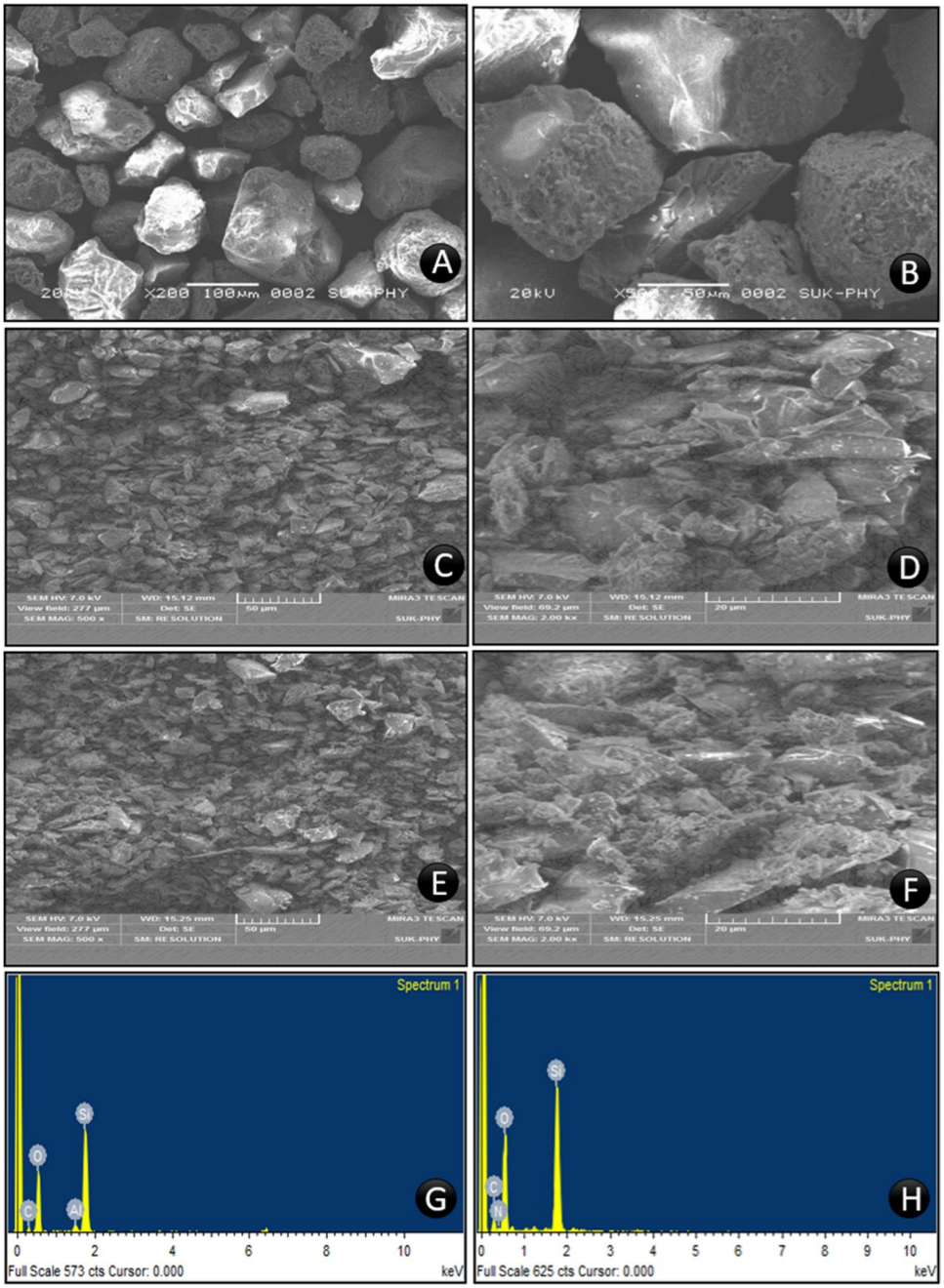

Fig. 1 FESEM images of waste sand particles (**A**, **B**), ASPs, (**C**, **D**) and AFSPs (**E**, **F**) and EDX spectra of (**G**) ASPs and (**H**) AFSPs

(Fig. 1 C and D) and AFSPs (Fig. 1 E and F). The FESEM images showed the formation of unevenly shaped particles with rough surfaces [38].

3.2 EDX Analysis

The EDX spectrum was used to determine the elemental compositions of the ASPs and AFSPs (Table 1). The EDX spectrum of ASPs showed major peaks for four elements, namely, Si, O, C, and Al (low) (Fig. 1 G). The EDX spectrum of AFSPs showed major peaks for Si, O and C with an

Table 1 Composition of sand particles

ASPs	Elements	Weight (%)	Atomic (%)
	Si	33.51	21.46
	O	52.64	59.17
	Al	1.66	1.10
	C	12.13	18.27
AFSPs	Si	21.63	13.71
	O	49.84	52.09
	C	17.53	23.24
	N	11.00	10.96

additional peak of N that confirmed successful amino functionalization (Fig. 1 H).

3.3 ATR-FTIR Analyses

The presence of amino groups on surface of sand particles in AFSPs was confirmed using ATR-FTIR spectroscopy. For AFSPs, four distinct peaks at approximately 1074, 1631, 781, and 1481 cm^{-1} (Fig. S3), which represent Si–O–Si stretching frequency, hydrogen bond peaks, and the presence of NH_2 groups (N–H bending) respectively. Spectral analyses of all three sand particles showed silanol groups on the surfaces of sand particles (shoulder at ~981 cm^{-1}). AFSPs showed two distinct absorption peaks, 2927 and 2922 cm^{-1} (CH stretching), confirming the presence of CH_2 groups. A similar peak at approximately 2927 cm^{-1} was observed in GSPs and ASPs. GSPs, ASPs, and AFSPs all showed a characteristic peak at approximately 1071 cm^{-1} (Si–O–Si bond of the siloxane backbone). This indicates that the GSPs retained the main backbone of sand after activation (ASPs) and functionalization (AFSPs) [39–41]. Spectral analysis was performed again after adsorption. The peak at 1621 cm^{-1} representing the O–H bending vibration mode of physisorbed water molecules was also observed. N–H stretching overlapped with the stretching vibrations of O–H groups at approximately 3484 cm^{-1}. Thus, hydrogen-bonded Si–OH and OH of physisorbed water molecules and the NH_2 groups were integrated into a broad peak at 3482 cm^{-1} [42].

3.4 TGA Analyses

TGA analysis was performed to further verify the presence of –OH and $–NH_2$ groups in ASPs and AFSPs. ASPs and AFSPs were gradually heated from 25 to 800 °C. AFSPs exhibited two steps of weight loss (Fig. S4). The first weight loss of 1.94% occurred at approximately 70 °C for ASPs and AFSPs. It was attributed to the physically adsorbed water molecules and ethanol. AFSPs clearly showed one further weight loss of 2.60% between 350 and 850 °C, and there was no weight loss in ASPs. This approximate 2% difference indicates the presence of an additional functional group, which is attributed to the presence of amino groups. The TGA results confirm that the surfaces of ASPs were successfully modified by APTES [39].

3.5 BET Surface Area Analyses

The surface area and porosities of materials are the primary factors that determine the adsorption capacity. BET surface area analyses revealed the specific surface area and pore size.

Using N_2 adsorption isotherms, adsorption curves for both ASPs and AFSPs were calculated [42]. The adsorption isotherms are presented in Fig. S5 which shows that the adsorption curves of all samples possess long straight line portions. At the starting point of the straight line, the adsorption is attributed to the capacity of the monolayer adsorption. For both ASPs and AFSPs, the long straight line portion of the adsorption curve was used to calculate the surface area [43]. Surface area analyses indicated that the specific surface area of the grafted sand (ASPs and AFSPs), as determined by the Brunauer–Emmett–Teller (BET) method, was 99.64 and 32.04 $m^2\ g^{-1}$ with pore volume and pore radius of 18.29 and 18.24(Å) respectively.

3.6 XRD Analysis

XRD analysis revealed the crystallinity of the ASPs and AFSPs, showing distinct diffraction peaks (Fig. 2). The characteristic peaks of ASPs were at 20.90°, 26.66°, 35.67°, 36.69°, 39.53°, 40.37°, 50.27°, 60.11°, 50.18°, 68.01°, 68.61°, while those of AFSPs were at 20.87°, 25.62°, 26.65°, 36.59°, 39.63°, 40.42°, 40.57°, 45.98°, 50.12°, 54.19°, 60.13°, 68.01°, and 68.39°. The absence of crucial intermediate peaks indicates the purity of sand particles, and the high peak intensities and sharpness of the XRD peaks indicate the good crystallinity [44]. The data matches with JCPDS (33–1161 card number) for silica quartz.

4 Use of Sand Particles as Dye Adsorbents

As ASPs and AFSPs are negatively (due to the presence of –OH groups) and positively (due to the presence of $–NH_2$ groups) charged respectively, their use as potent adsorbents for cationic and anionic dyes was hypothesized. Cationic and anionic dyes typically have high affinities toward negatively

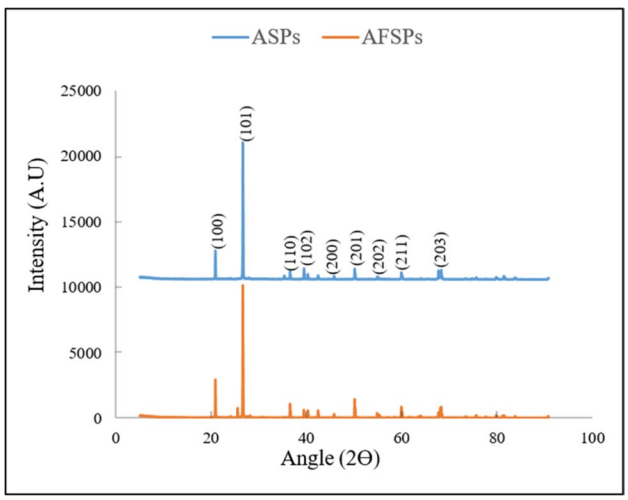

Fig. 2 XRD analysis of ASPs and AFSPs

and positively charged groups. Thus, cationic and anionic dyes get adsorbed on ASPs and AFSPs because of negatively charged surface –OH groups and positively charged NH_2 groups respectively.

4.1 Optimization of Adsorbent Amounts

The first step for utilizing ASPs and AFSPs as adsorbents was to determine the lowest possible adsorbent amount to achieve quantitative removal of dyes. Cationic MB and anionic MO dyes were used (120 min, 550 rpm on a magnetic stirrer) to determine the optimum adsorbent amounts of ASPs and AFSPs, respectively. We started with 0.1 g adsorbent amount and gradually increased it to 0.250 g where satisfactory adsorption was achieved. With increase in the amounts of ASPs and AFSPs, the percentage removal of MB and MO increased. For 0.250 g of ASPs and AFSPs, the percentage removal of MB and MO was up to 99.99 and 99.78% (Fig. S6). Thus, the absorbent amount was fixed at 0.250 g for subsequent experiments. These optimized conditions for maximum adsorption are shown in Table S4.

4.2 Dye Removal Efficiency of ASPs and AFSPs

The experimental parameters (0.250 g, 120 min, 550 rpm) were determined and the adsorption removal was tested using ASPs and AFSPs for different cationic dyes such as MB, MG, MV, and Rh B and anionic dyes such as MO, PB VF, QY, and RR 2. The concentrations of the dyes were determined using UV–visible spectroscopy. The solutions of cationic dyes showed visible change in color after the adsorption experiments (Fig. 3A, B, C and D). We observed that the color of MB, MG, MV and Rh B solutions changed from dark sky blue, violet, blue and pink turned to colorless indicating complete adsorption. In all the adsorption experiments, the decrease in absorbance maxima for MB, MG, MV and Rh B were analyzed at 664, 617, 590, 556 nm indicated that adsorption was increased with time. Similarly, the anionic dyes showed visible changes in color after adsorption experiments (Fig. 4A, B, C and D). We observed that the color of MO, PB VF, QY, and RR 2 solutions changed from orange, dark sky blue, yellow, red turned to colorless indicating complete adsorption. In all the adsorption experiments, the decrease in absorbance maxima of MO, PB VF, QY and RR 2 were analyzed at 466, 636, 412, and 539 nm indicate that adsorption was increased with time.

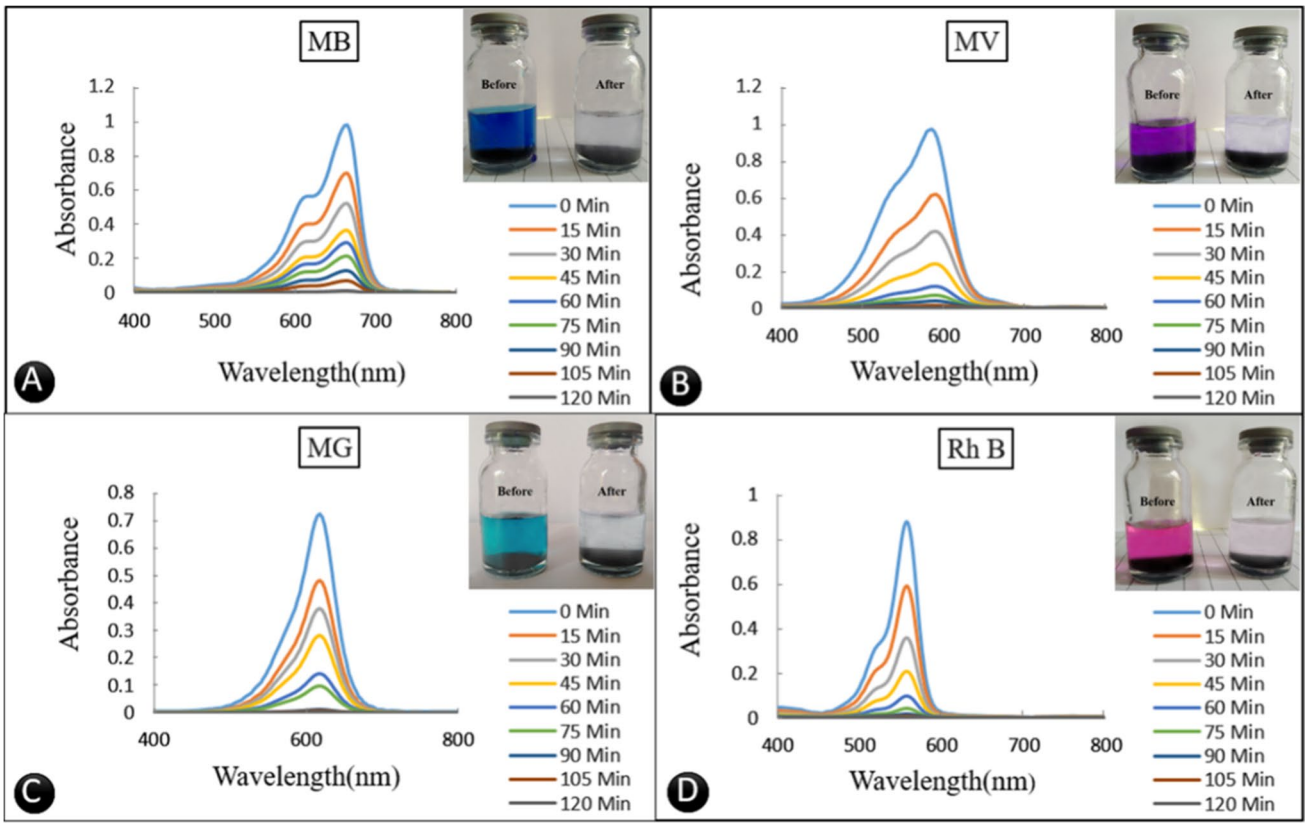

Fig. 3 UV–visible absorption spectra of cationic dye solutions at different time intervals: (**A**) MB, (**B**) MG, (**C**) MV, and (**D**) Rh B at pH 7.3 and time 120 min

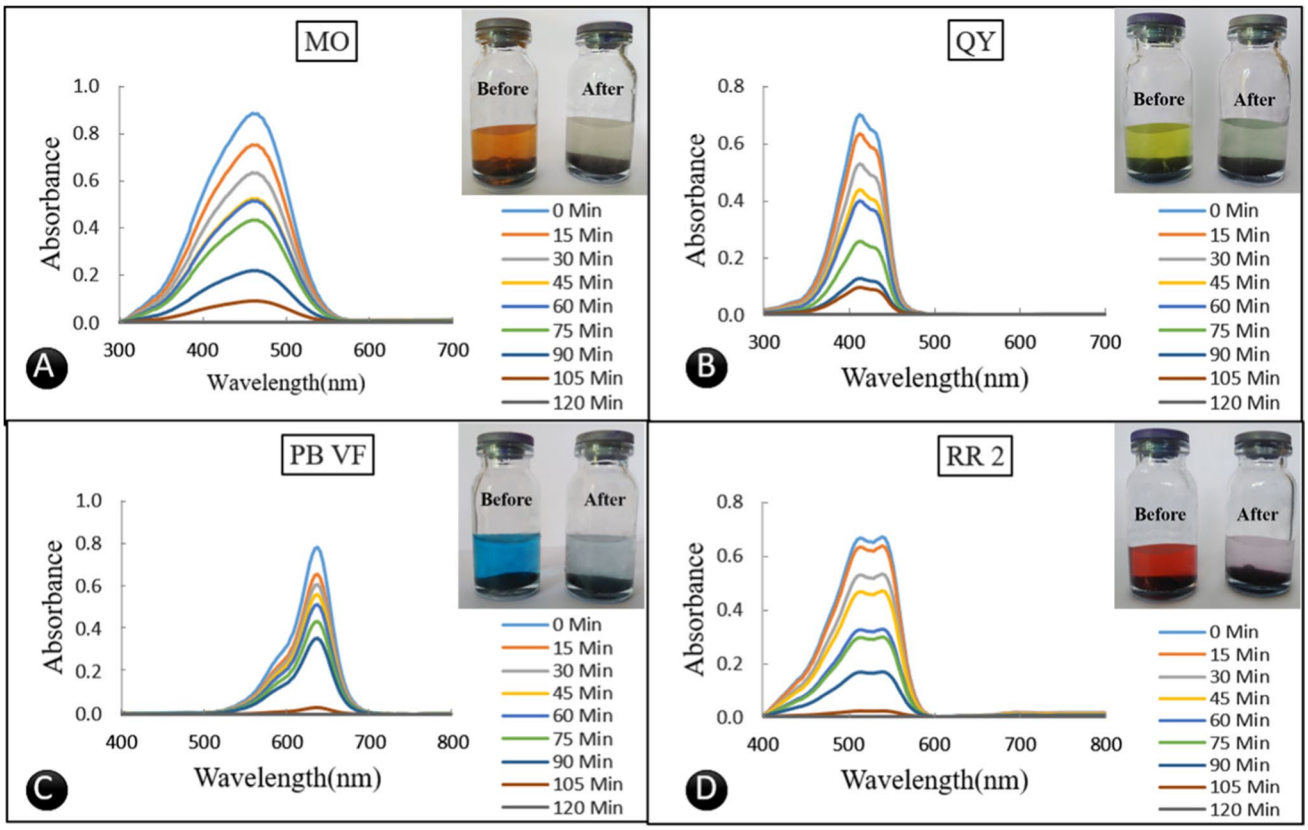

Fig. 4 UV–visible absorption spectra of anionic dye solutions at different time intervals: (**A**) MO, (**B**) PB VF, (**C**) QY, and (**D**) RR2 at pH 6.9 and time 120 min

Using these absorbance values, equilibrium concentrations of dyes were determined. The adsorbents at equilibrium time was calculated using the following equation [45]:

$$\%\ \text{Removal efficiency} = \frac{(\text{Co} - \text{Ce})}{\text{Co}} \text{x} 100 \tag{1}$$

Co and Ce are the initial and equilibrium concentrations of dyes, respectively. The removal efficiencies of cationic and anionic dyes are shown in Fig. 5 and 6, respectively. The data shows removal efficiency of cationic dyes such as MB, MG, MV and Rh B were 99.99, 99.57, 99.59, and 99.69% and for anionic dyes such as MO, PB VF, QY, and RR 2 were 99.78, 99.87, 99.86 and 99.98% respectively.

4.3 Adsorption Isotherms of ASPs and AFSPs for Dyes

The ASPs and AFSPs can achieve quantitatively dye removal efficiencies, the adsorption capacities was determined. For this purpose four different adsorption isotherms models namely, Langmuir, Freundlich, Temkin, and Elovich were tested.

4.3.1 Langmuir Isotherms

The Langmuir isotherm model is best suited for the homogeneous surface formation of monolayer with no interaction between the adsorbed ions. Langmuir adsorption isotherm is expressed using Eq. (2) [46]:

$$\frac{Ce}{qe} = \frac{Ce}{qm} + \frac{1}{K_L qm} \tag{2}$$

where q_m (mg g^{-1}) is the maximum adsorption capacity, K_L (L mg^{-1}) is the Langmuir constant, q_e is the equilibrium amount, and C_e is the equilibrium concentration. Values of qm and Langmuir constant K_L were calculated from the C_e/q_e vs. plot (C_e with $1/q_m$ slope and $1/K_L q_m$ intercept). Langmuir dimensionless separation factor R_L was determined using Eq. (3):

$$R_L = \frac{1}{1 + K_L C_e} \tag{3}$$

The value of R_L is between 0 and 1, it indicates favorable adsorption, $R_L > 1$ indicates unfavorable adsorption, $R_L = 1$

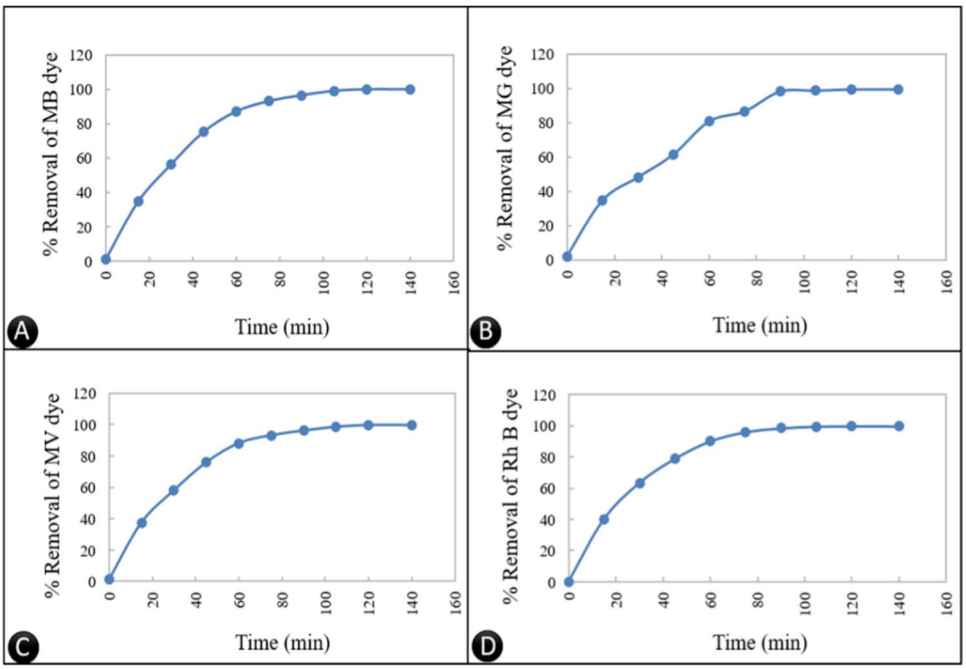

Fig. 5 Dye removal efficiencies of cationic dyes upon interaction with ASPs: (**A**) MB, (**B**) MG, (**C**) MV, and (**D**) RhB at pH 7.3 and time 140 min

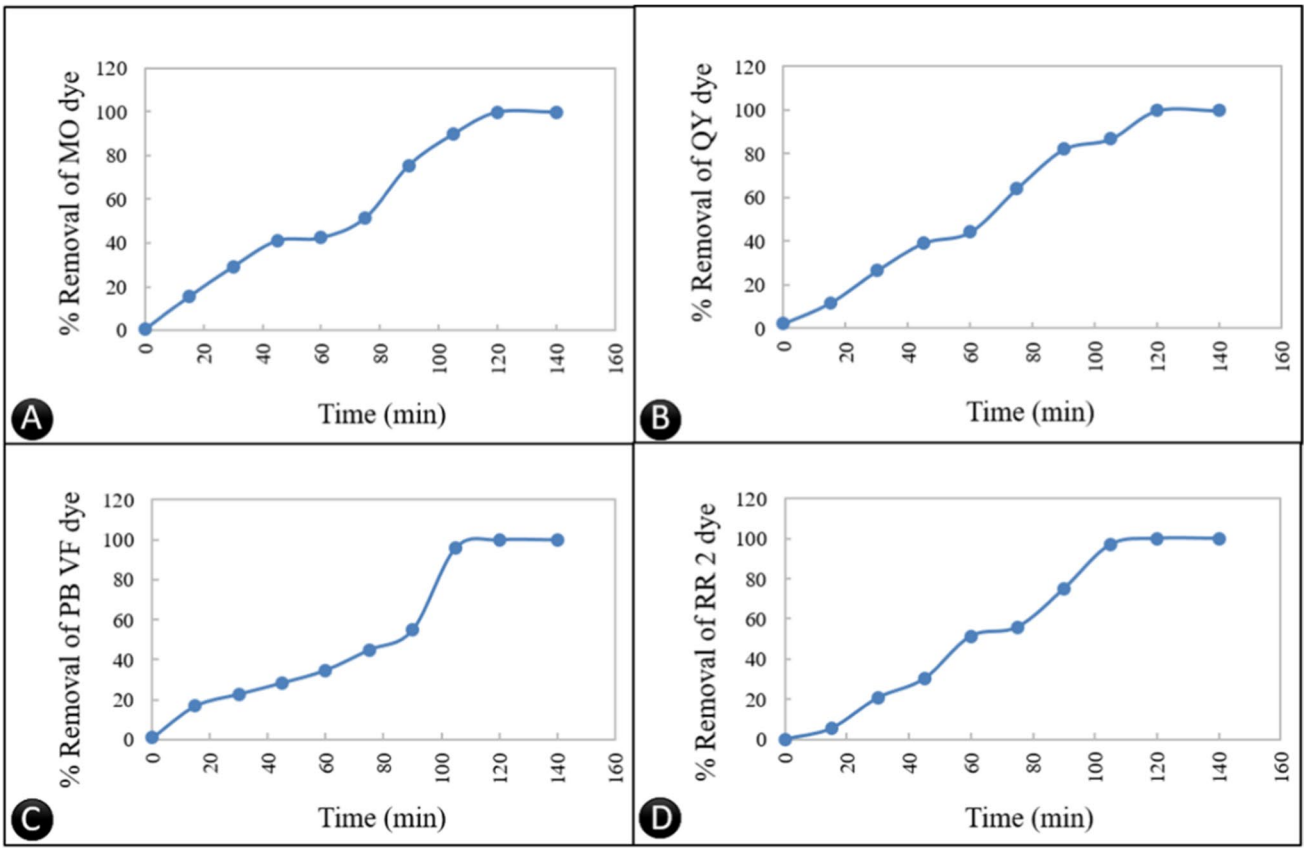

Fig. 6 Dye removal efficiencies of anionic dyes upon interaction with AFSPs: (**A**) MO, (**B**) PB VF, (**C**) QY, and (**D**) RR2 at pH 6.9 and time 140 min

indicates linear adsorption, and $R_L = 0$ indicates an irreversible adsorption process.

4.3.2 Freundlich Isotherm

The Freundlich isotherm model is best suited for heterogeneous surfaces where adsorption is multi-layered, with different energies for different adsorption sites. The linear form of Freundlich isotherm is expressed using Eq. (4) [23]:

$$lnqe = lnkf + \frac{1}{n}(lnCe) \tag{4}$$

where K_f (L g^{-1}) is the Freundlich constant related to the adsorption capacity and n indicates the intensity of adsorption, qe (mg g^{-1}) and C_e (mg L^{-1}) are the amount adsorbed and equilibrium concentration of cationic dyes such as MB, MG, MV, and Rh B and anionic dyes such as MO,PB VF, QY, and RR 2.

4.3.3 Temkin Isotherm

The Temkin isotherm model focuses on the indirect interactions between adsorbate and adsorbent; it represents linear reduction in the energy based on coverage. The Temkin isotherm clarifies the circuitous associations between the adsorbate and the adsorbent. These interactions lead to linear decrease in the heat of molecules in the adsorbate layer with coverage. The Temkin adsorption isotherm is expressed using Eq. (5) [23]:

$$qe = \frac{RT}{b} lnK_T + \frac{RT}{b} lnC_e \tag{5}$$

where K_T (L mg^{-1}) is the equilibrium binding constant corresponding to the maximum binding energy, b is the heat of adsorption, R is the universal gas constant, and q_e and C_e are the equilibrium amount and equilibrium concentration respectively. The plot of q_e vs. lnC_e yielded a linear, from its slope and intercept the constant K_T and b were evaluated.

4.3.4 Elovich Isotherm

The Elovich isotherm is expressed as a multilayer adsorption system, and the Elovich adsorption isotherm is expressed using Eq. (6) [23]:

$$ln\left(\frac{q_e}{C_e}\right) = ln\left(K_{Eq_m}\right) - \frac{1}{q_m} q_e \tag{6}$$

where K_E is the Elovich constant; the maximum adsorption capacity can be calculated from the graph of ln (q_e/C_e) vs. q_e using the intercept and slope.

4.4 Adsorption Capacities for ASPs and AFSPs

The most suitable isotherm model is determined by the linear regression coefficient (R^2). The value of R^2 closer to 1 indicates the most suitable isotherm model. We calculated isotherm constant values using the slopes and intercepts to identify the adsorption mechanism and calculate the adsorption capacity (Tables 2 and 3 for cationic and anionic dyes respectively).For both anionic and cationic dyes, among all four isotherm models, the Langmuir model showed the highest values of R^2, indicating monolayer adsorption. Other isotherm models were excluded as they show deviations from linear graphs (a higher number of intercepts away from the trend line).The adsorption capacity of ASPs for MB was calculated as 38.16 mg g^{-1} using Langmuir isotherm ($R^2 = 0.99$). The Langmuir model showed a straight line from 0 to 3.4 mg L^{-1} (Fig. S7 A). Other isotherm models showed deviations from the linear graph (Fig. S7 B, C, and D). The adsorption capacity of

Table 2 Isotherm constants of adsorption of cationic dyes on ASPs

Dyes	Langmuir		Freundlich		Temkin		Elovich	
Methylene Blue (MB)	K_L (L mg^{-1})	0.134	K_F (L g^{-1})	35.58	K_T (L mg^{-1})	2.9579×10^{11}	K_E (L mg^{-1})	7.0274×10^{54}
	q_m (mg g^{-1})	38.16	n	40.0	B	0.041	q_m(mg g^{-1})	0.132
	R^2	0.9962	R^2	0.9725	R^2	0.9598	R^2	0.9601
Malachite Green (MG)	K_L (L mg^{-1})	0.14	K_F (L g^{-1})	35.49	K_T (L mg^{-1})	7.79574×10^{41}	K_E(L mg^{-1})	1.21973×10^{47}
	q_m (mg g^{-1})	26.31	n	28.57	B	0.051	q_m(mg g^{-1})	0.047
	R^2	0.965	R^2	0.9543	R^2	0.8057	R^2	0.724
Methyl Violet (MV)	K_L (L mg^{-1})	0.08	K_F (L g^{-1})	73.28	K_T (L mg^{-1})	2.1544×10^{50}	K_E (L mg^{-1})	2.5998×10^{66}
	q_m (mg g^{-1})	55.24	n	24.75	B	0.059	q_m(mg g^{-1})	0.047
	R^2	0.9951	R^2	0.9798	R^2	0.9783	R^2	0.8023
Rhodamine B (RhB)	K_L (L mg^{-1})	0.09	K_F (L g^{-1})	34.88	K_T (L mg^{-1})	1.6213×10^{25}	K_E(L mg^{-1})	3.89022×10^{37}
	q_m (mg g^{-1})	35.84	n	24.94	B	0.084	q_m(mg g^{-1})	0.06
	R^2	0.9949	R^2	0.9638	R^2	0.9249	R^2	0.9541

Table 3 Isotherm constants of adsorption of anionic dyes on AFSPs

Dyes	Langmuir		Freundlich		Temkin		Elovich	
Methyl Orange (MO)	K_L (L mg^{-1})	1.361	K_F (L g^{-1})	178.1	K_T (L mg^{-1})	6.2364×10^{22}	K_E (L mg^{-1})	5.69202×10^{47}
	q_m (mg g^{-1})	7.28	n	54.05	B	0.1808	q_m(mg g^{-1})	0.092
	R^2	0.953	R^2	0.917	R^2	0.9139	R^2	0.58
Patent Blue VF (PB VF)	K_L (L mg^{-1})	1	K_F (L g^{-1})	37.33	K_T (L mg^{-1})	3.705×10^{57}	K_E(L mg^{-1})	9.38303×10^{34}
	q_m (mg g^{-1})	4.63	n	60.98	B	0.037	q_m(mg g^{-1})	0.064
	R^2	0.927	R^2	0.803	R^2	0.6204	R^2	0.466
Quinoline Yellow (QY)	K_L (L mg^{-1})	1.244	K_F (L g^{-1})	179.7	K_T (L mg^{-1})	1.12696×10^{25}	K_E (L mg^{-1})	5.19307×10^{38}
	q_m (mg g^{-1})	7.84	n	60.61	B	0.166	q_m(mg g^{-1})	0.115
	R^2	0.97	R^2	0.873	R^2	0.913	R^2	0.806
Reactive Red 2 (RR2)	K_L (L mg^{-1})	7.266	K_F (L g^{-1})	71.01	K_T (L mg^{-1})	2.41437×10^{31}	K_E(L mg^{-1})	$2.56637E\times10^{14}$
	q_m (mg g^{-1})	6.91	n	80.65	B	0.652	q_m(mg g^{-1})	1.501
	R^2	0.952	R^2	0.761	R^2	0.847	R^2	0.229

ASPs for MG was calculated as 26.31 mg g^{-1} using Langmuir isotherm ($R^2=0.97$). The Langmuir model showed a straight line from 0 to 2.0 mg L^{-1} (Fig. S8 A). Other isotherm models show deviations from the linear graph (Fig. S8 B, C, and D). The adsorption capacity of ASPs for MV was calculated as 55.24 mg g^{-1} using Langmuir isotherm ($R^2=0.99$). The Langmuir model shows a straight line from 0 to 4.5 mg L^{-1} (Fig. S9 A). Other isotherm models showed deviations from the linear graph (Fig. S9 B, C, and D). The adsorption capacity of ASPs for Rh B was calculated as 35.84 mg g^{-1} using Langmuir isotherm ($R^2=0.99$). The Langmuir model showed a straight line from 0 to 3 mg L^{-1} (Fig. S10 A). Other isotherm models showed deviations from the linear graph (Fig. S10 B, C, and D). The collective results are shown in Table S4.

Similarly, the adsorption capacity of AFSPs for MO was calculated as 7.28 mg g^{-1} using Langmuir isotherm ($R^2=0.95$). The Langmuir model showed a straight line from 4.5 to 8.5 mg L^{-1} (Fig. S11 A). Other isotherm models showed deviations from the linear graph (Fig. S11 B, C, and D). The adsorption capacity of AFSPs for PB VF calculated as 4.63 mg g^{-1} using Langmuir isotherm ($R^2=0.92$). The Langmuir model showed a straight line from 0 to 4.3 mg L^{-1} (Fig. S12 A). Other isotherm models showed deviations from the linear graph (Fig. S12 B, C, and D). The adsorption capacity of AFSPs for QY was calculated as 7.84 mg g^{-1} using Langmuir isotherm ($R^2=0.97$). The Langmuir model showed a straight line from 6 to 9 mg L^{-1} (Fig. S13 A). Other isotherm models showed deviations from the linear graph (Fig. S13 B, C, and D). The adsorption capacity of AFSPs for RR 2 was calculated as 6.91 mg g^{-1} using Langmuir isotherm ($R^2=0.95$). The Langmuir model showed a straight line from 6 to 9 mg L^{-1} (Fig. S14 A). Other isotherm models showed deviations from the linear graph (Fig. S14 B, C, and D). The collective results are shown in Table S4.

4.5 Kinetic Study of Dyes

The adsorption capacities of ASPs and AFSPs for individual dyes were calculated, and the adsorption mechanism was determined using kinetic models. Two kinetic models were used to study the uptake rate of cationic dyes on ASPs and anionic dyes on AFSPs, namely, pseudo-first-order (Lagergren, 1898, Y.S. Ho, 2004; Eq. (7)) [27], and pseudo-second-order (8) [27], kinetic models.

$$log(q_e - q_t) = log(q_e) - \left(\frac{K_1}{2.303}\right)t \tag{7}$$

where q_e and q_t (mg g^{-1}) represent the amount of dye adsorbed at equilibrium and at time t, and k_1 (min^{-1}) is the rate constant. The plot of log (q_e—q_t) versus t gives the values of k_1,

$$\frac{t}{q_t} = \frac{1}{k_2 q_e^2} + \left(\frac{1}{q_e}\right)t \tag{8}$$

where the amount of dye adsorbed at equilibrium and at time t is qe and qt, respectively. K_2 is the pseudo-second-order rate constant (g mg^{-1} min^{-1}). The values of K_2 and q_e for the pseudo-second-order model were determined from the intercept and the slope of the plot of t/q_t vs. t. This equation does not consider the concentration of the adsorbate, and the adsorption rate depends only on the adsorption capacity. In such cases, chemisorption is considered as the rate-limiting step.

Similar to determining the adsorption capacities of the ASPs and AFSPs for different dyes, kinetic equations and coefficient values (R^2) were calculated. This implies that the pseudo-second-order kinetic model showed values of R^2 closer to 1 for all cationic and anionic dyes (Tables S1 and S2, respectively). The Fig. S15–S22A and B represent the pseudo-first-order and pseudo-second-order

kinetic model graphs, respectively; clearly, more intercepts are seen on the line graph for the pseudo-second-order kinetic model. Thus, we confirm that the pseudo-second-order model was the most suitable for the adsorption kinetics ($R^2 = 0.99$).

4.6 Reusability of the Adsorbent (Desorption Experiment Result)

The findings of this study confirmed that ASPs and AFSPs are suitable for adsorbing various dyes. To determine the reusability of the particles, ASPs and AFSPs used in the adsorption capacity measurement experiment were tested for several adsorption cycle. To reuse adsorbent, adsorbed dyes on the surfaces of ASPs and AFSPs were removed by extraction in ethanol. The leached dye concentrations were checked by using a UV–visible spectrophotometer. Experimental results of the desorption experiments were exactly opposite to those of the adsorption experiments (Fig. 7 and 8). Both cationic and anionic dyes were recovered using ethanol which is the best solvent for the dyes. To determine the reusability of the sand derived adsorbents, the entire process of adsorption–desorption was repeated for five times using the same sand particles. The regeneration study was conducted for one adsorption experiment were reused up to five cycles for adsorption removal of dyes (Figs S23 and S24 for ASPs and AFSPs, respectively).This proved that the ASPs and AFSPs are excellent reusable adsorbents for cationic and anionic dyes.

5 Use of AFSPs as Adsorbent for Removal Metal Ions

The testing of AFSPs for removal of metal ions, we choose Cd(II), Ni(II), Co(II), and Cr(VI) as model pollutants due to their common occurrence and toxic nature. Keeping the experimental conditions same as those for adsorption of dyes for metal ions (0.250 g, 180 min, 550 rpm on a magnetic stirrer), adsorption removal efficiencies of AFSPs were calculated. Similar to dyes, the amount of metal ions adsorbed on the surface of AFSPs increased with time. The removal efficiencies using fresh AFSPs was ranged between 60–100% (Fig. S25) for selected metal ions. The metal removal efficiency at equilibrium time was calculated using Eq. (9):[45]

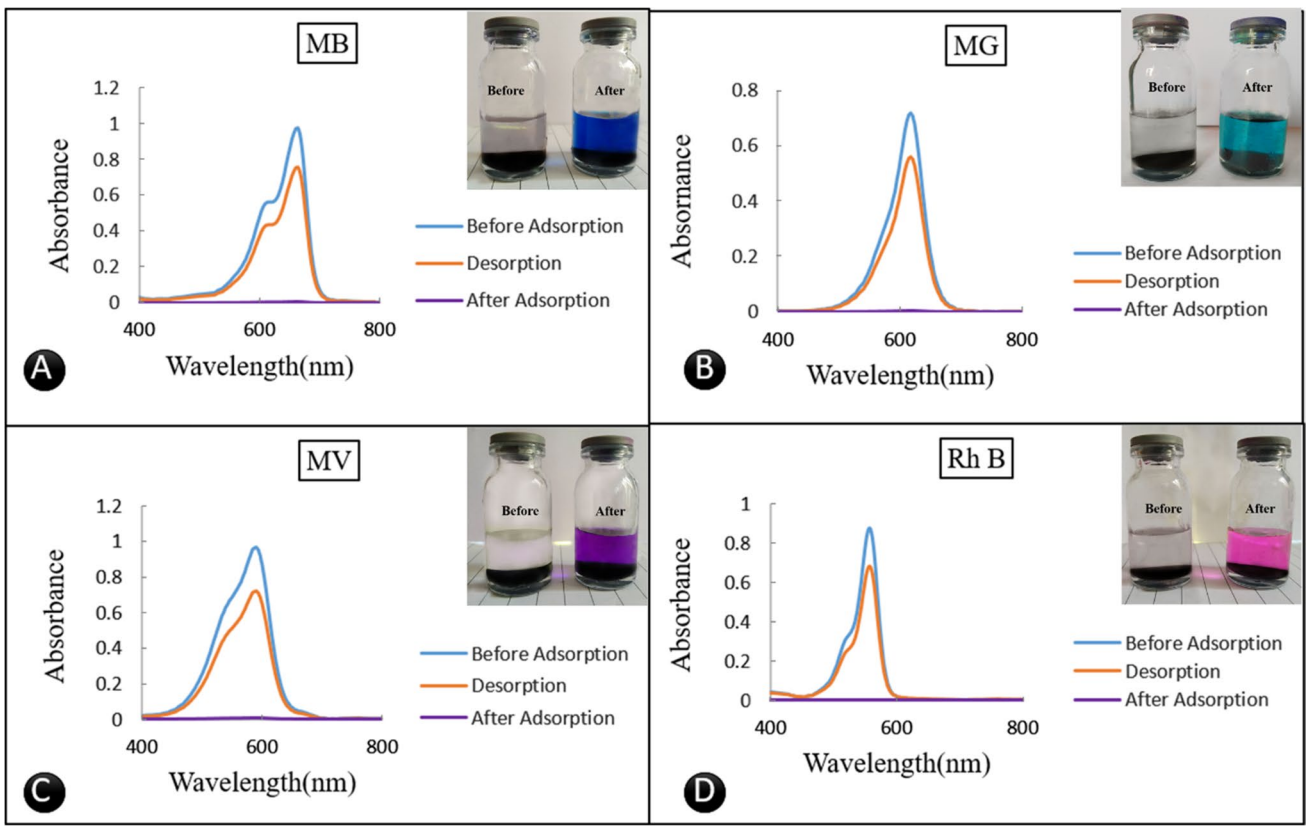

Fig. 7 Recovery of dyes after adsorption removal (**A**) MB, (**B**) MG, (**C**) MV, and (**D**) Rh B from ASPs

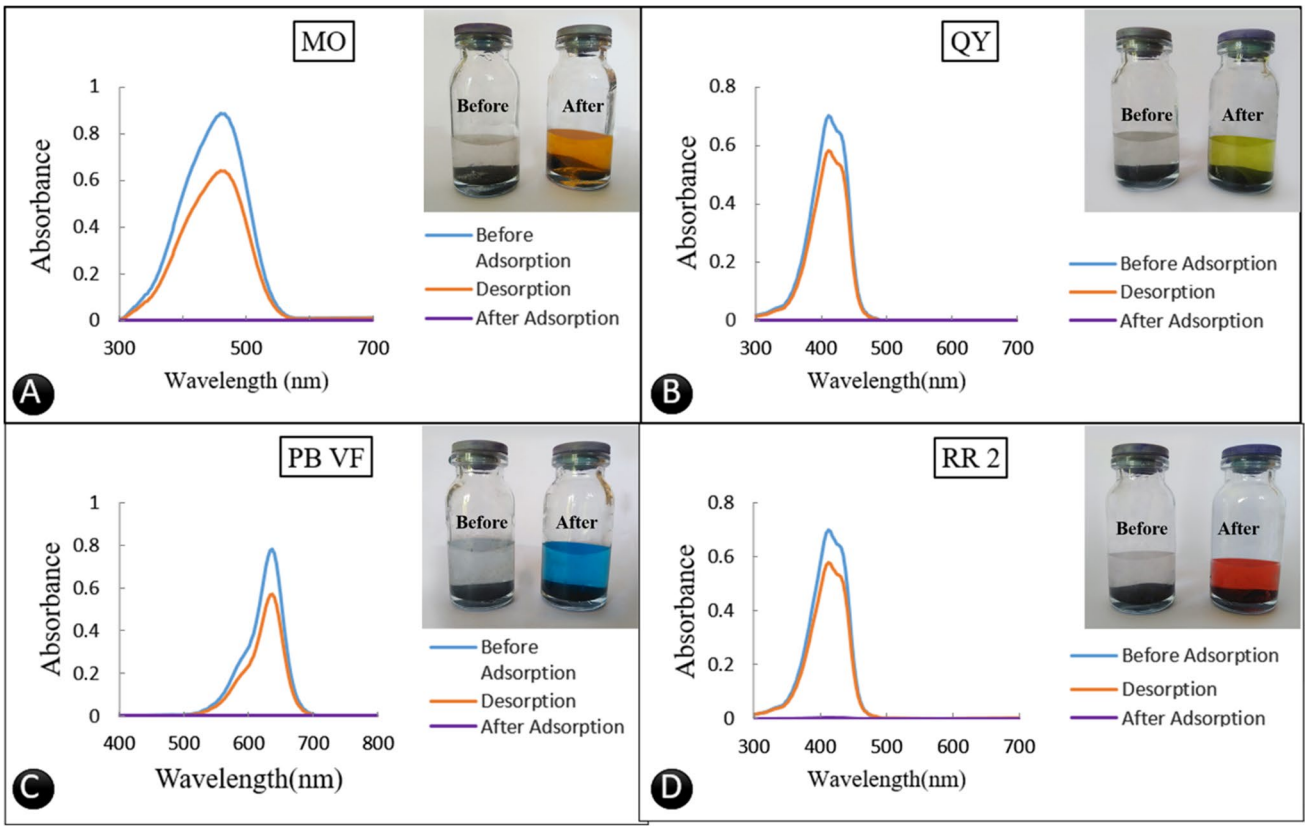

Fig. 8 Recovery of dyes after adsorption removal (**A**) MO, (**B**) PB VF, (**C**) QY, and (**D**) RR2 from AFSPs

$$\%\text{Removal efficiency} = \frac{(\text{Co} - \text{Ce})}{\text{Co}} \text{x} 100 \quad (9)$$

where Co and Ce are the initial and equilibrium concentrations of metal ions respectively. The metal ions Cd(II), Ni(II), Co(II), and Cr(VI) were 100, 95.71, 98.50 and 56.14% respectively. The optimized conditions for maximum adsorption are shown in Table S4.

5.1 Adsorption Isotherms Study of Metal Ions

Adsorption isotherm models were applied for metal ion adsorption to determine the adsorption capacities of AFSPs. Linear graph intercepts were considered for calculating the coefficient of variation (R^2). Similar to dyes, among all four isotherm models, Langmuir model showed the highest values for R^2, which is also evident from the isotherm plots indicating a monolayer adsorption process. We calculated isotherm constant values using the slopes and intercept to identify the adsorption mechanism and calculated the adsorption capacities (Table 4).

The adsorption capacity of AFSPs for Cd was calculated as 23.81 mg g^{-1} using Langmuir isotherm ($R^2 = 0.97$). The Langmuir model showed a straight line from 0 to 2.6 mg L^{-1} (Fig. S26 A). Other isotherm models showed deviations from the linear graph (Fig. S26 B, C and D). The adsorption capacity of AFSPs for Ni was calculated as 43.06 mg g^{-1} using Langmuir isotherm ($R^2 = 0.95$). The Langmuir model showed a straight line from 0 to 7.9 mg L^{-1} (Fig. S27 A). Other isotherm models showed deviations from the linear graph (Fig. S27 B, C and D). The adsorption capacity of AFSPs for Co was calculated as 17.03 mg g^{-1} using Langmuir isotherm ($R^2 = 0.97$). The Langmuir model showed a straight line from 0 to 9 mg L^{-1} (Fig. S28 A). Other isotherm models showed deviations from the linear graph (Fig. S28 B, C and D). The adsorption capacity of AFSPs for Cr was calculated as 3.47 mg g^{-1} using Langmuir isotherm ($R^2 = 0.97$). The Langmuir model showed a straight line from 4.3 to 9.2 mg L^{-1} (Fig. S29 A). Other isotherm models showed deviations from the linear graph (Fig. S29 B, C and D). The collective results are shown in Table S5.

5.2 Kinetic Study of Metal Ions

Similar to the adsorption of dyes, both kinetic models were studied for the adsorption of metal ions. Pseudo-first-order

Table 4 Langmuir, Freundlich, Temkin and Elovich isotherm parameters for metal ion adsorption by AFSPs

Metal ions	Langmuir		Freundlich		Temkin		Elovich	
Cadmium (II)	K_L (L mg^{-1})	0.1836	K_F (L g^{-1})	156.24	K_T (L mg^{-1})	3.13×10^{14}	K_E (L mg^{-1})	$5.495\times10^{+4}$
	q_m (mg g^{-1})	23.81	n	34.84	B	0.285	q_m(mg g^{-1})	0.5098
	R^2	0.9671	R^2	0.9188	R^2	0.9165	R^2	0.9212
Nickel (II)	K_L (L mg^{-1})	0.2437	K_F (L g^{-1})	1.1256	K_T (L mg^{-1})	1.0492	K_E(L mg^{-1})	$4.8027\times10^{+4}$
	q_m (mg g^{-1})	43.06	n	2.16	B	8.8698	q_m(mg g^{-1})	0.5755
	R^2	0.9710	R^2	0.907	R^2	0.9663	R^2	0.9694
Cobalt (II)	K_L (L mg^{-1})	0.271	K_F (L g^{-1})	85.507	K_T (L mg^{-1})	67.09515	K_E (L mg^{-1})	$1.91\times10^{+5}$
	q_m (mg g^{-1})	17.03	n	6.2112	B	1.538	q_m(mg g^{-1})	0.8332
	R^2	0.9403	R^2	0.7957	R^2	0.7895	R^2	0.9109
Chromium (VI)	K_L (L mg^{-1})	3.42	K_F (L g^{-1})	158.49	K_T (L mg^{-1})	8.1517×10^{21}	K_E(L mg^{-1})	$1.91\times10^{+5}$
	q_m (mg g^{-1})	3.47	n	52.632	B	0.179	q_m(mg g^{-1})	0.8331944
	R^2	0.9987	R^2	0.7925	R^2	0.7888	R^2	0.8169

and pseudo-second-order kinetic model graphs are shown in Figs. S30–S33 A and in Figs. S30–S33 B respectively. Table S3 shows the values for the metal ions obtained from the slopes and intercepts. The adsorption process followed the pseudo-second-order kinetic model ($R^2=0.99$). Thus, chemisorption was considered the rate-limiting step.

5.3 Elemental Composition of AFSPs After Adsorption

During EDX analysis, it was confirmed that the elemental composition of AFSPs shows Si, O, and C, and an additional peak of N. The same characterization was carried out to verify the adsorbed metal ions. The EDX spectrum for Cd demonstrates two additional sharp peaks at 3.3 and 4.1 keV corresponding to Cd (Fig. 9A). Compared with standard AFSPs spectrum, subsequent increase in C, Si, and O was observed. Low quantities of Na and Cd were also seen. This result revealed that the adsorption of Cd also triggered the adsorption of other metal ions.

Similar to Cd, the EDX spectrum for Co showed an additional peak at 0.9 keV (Fig. 9B). The composition of sand particles after adsorption of metal ions is shown in Table 5.

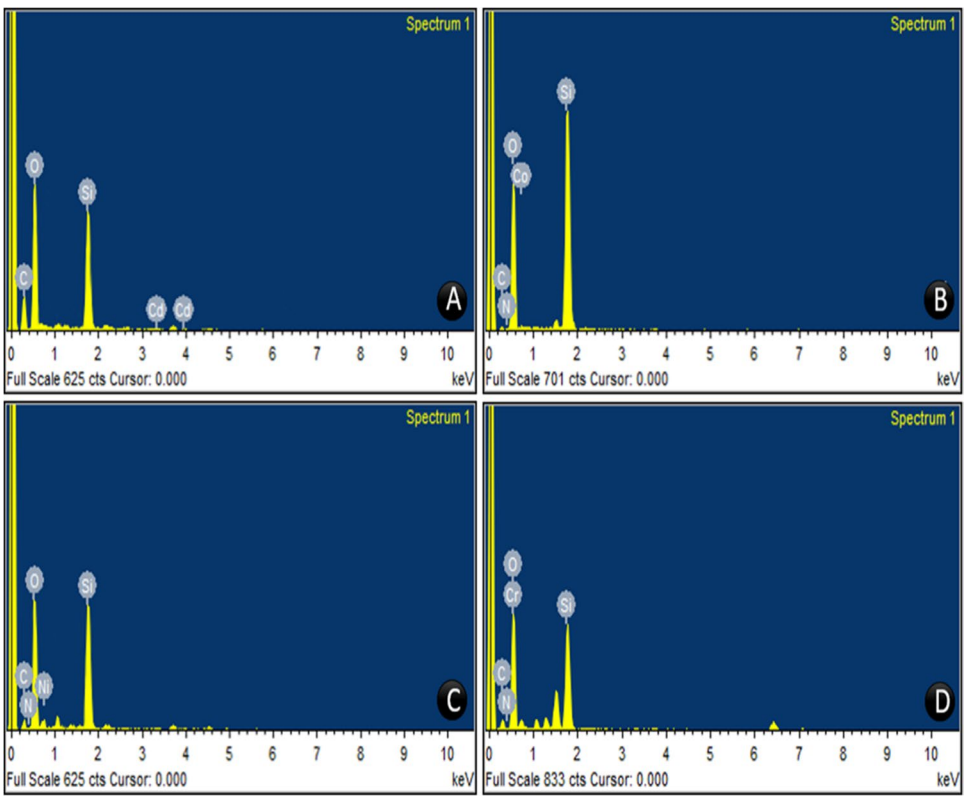

Fig. 9 EDX spectra of (**A**) AFSPs after adsorption of Cd (II), (**B**) AFSPs after adsorption of Co (II), (**C**) AFSPs after adsorption of Ni (II), and (**D**) AFSPs after adsorption of Cr (VI)

Table 5 Composition of sand particles after adsorption of metal ions

	Elements	Weight (%)	Atomic (%)
AFSPs -after adsorption of Cd(II)	Si	15.13	8.74
	O	47.41	51.47
	N	4.45	1.10
	C	22.71	32.84
	Cd	10.30	5.85
AFSPs- after adsorption of Co(II)	Si	32.14	21.41
	O	55.13	64.47
	N	3.97	5.30
	C	4.55	7.09
	Co	4.21	1.73
AFSPs -after adsorption of Ni(II)	Si	19.29	12.50
	O	50.98	57.99
	N	5.30	6.88
	C	9.95	15.07
	Ni	14.48	7.93
AFSPs -after adsorption of Cr(VI)	Si	19.59	11.58
	O	62.06	64.40
	N	6.18	7.32
	C	12.06	16.66
	Cr	0.11	0.04

The EDX spectrum of Ni showed an additional peak at 0.8 keV (Fig. 9C). The EDX spectrum for Cr also showed a corresponding peak at 0.8 keV (Fig. 9D).

5.4 Reusability of AFSPs as Adsorbents for Metals

The study of adsorbents was conducted successfully for five cycles with 60–100% ± 0.24% adsorption efficiency (Fig. S34) using adsorption–desorption cycles of AFSPs. For every cycle, the adsorbent was reused by washing with slightly basic water. No considerable loss in adsorption capacity confirmed the reusability of AFSPs as potent adsorbents for metal ions.

6 Conclusions

WFS-derived adsorbents prepared by size reduction followed by functionalization showed excellent adsorption efficiencies against various types of pollutants such as cationic and anionic dyes and heavy metal ions. Almost quantitative removal of most of the model pollutants used was achieved. The equilibrium data were well described in the Langmuir model, indicating monolayer adsorption. Kinetic data were adequately fitted by the pseudo-second-order kinetic model, predicting chemisorption as the adsorption mechanism. The success of adopting any experimental procedure on an industrial scale depends on the easy procurement and processing of raw materials, ease of maintaining operational parameters, and optimal use of key materials. High removal efficiencies and adsorption at room temperature are essential factors for industrial adoption for effluent treatment process. The adsorbent materials developed in this work are reusable without substantial loss of removal efficiencies. Thus, ASPs and AFSPs are potentially good alternative adsorbents for low-cost water purification technology, especially for industries where effluents have to be processed throughout the day. The proposed method supports circular economy, waste reduction and the idea of best from waste. The potential applications of the materials developed in this study can be extended to remove various other dyes and metal ions as well as pollutants from other classes from water.

Abbreviations *ASPs*: Activated sand particles; *AFSPs*: Amino functionalized sand particles; *ATR-FTIR*: Attenuated Total Reflection Fourier Transforms Infrared; *BET*: Brunauer-Emmett-Teller; *EDX*: Energy Dispersive X-Ray Analysis; *FESEM*: Field Emission Scanning Electron Microscopy; *GSPs*: Grinded sand particles; K_E: Elovich Constant; K_F: Freundlich isotherm Constant; K_L: Langmuir constant; K_T: Temkin Constant; *MB*: Methylene Blue; *MG*: Malachite Green; *MO*: Methyl Orange; *MV*: Methyl Violet; *n*: Dimensionless reaction order; *PB VF*: Patent Blue VF; q_m: Maximum adsorption capacity; *QY*: Quinoline Yellow; R^2: Correlation Coefficients; *Rh B*: Rhodamine B; *RR 2*: Reactive Red 2; *TGA*: Thermo gravimetric Analysis; *XRD*: X-ray diffraction

Supplementary Information The online version contains supplementary material available at https://doi.org/10.1007/s12633-023-02383-w.

Acknowledgements Author H.B Garud is thankful to Chhatrapati Shahu Maharaj Research Training and Human Development Institute (SARTHI), Pune (India) for financial support through Chhatrapati Shahu Maharaj National Research Fellowship (CSMNRF)

Authors' Contributions **Harshada Garud**: Investigation, Methodology, Data curation and Writing—Original Draft **Sushilkumar Jadhav**: Conceptualization, Methodology, Supervision, Resources & Writing—Review & Editing **Sayali Jadhav**: Investigation, Methodology and Writing—Original Draft **Pradnya Suryawanshi**: Investigation and Data curation **Vilas Kalantre**: Supervision and Resources **Shivaji Burungale**: Supervision & Resources **Sagar Delekar**: Resources **Pramod Patil**: Supervision & Resources. All authors read and approved the final manuscript.

Funding The authors declare that no funds, grants, or other support were received during the preparation of this manuscript.

Data Availability Data and materials supporting the research are found within the manuscript.

Declarations

Ethics Approval Authors approve that the submitted work is original and has not been published elsewhere in any form or language (partially or in full).

Consent to Participate Not applicable.

Consent for Publication All authors provided their consent for the publication.

Competing interests The authors declare no competing interests.

References

1. Ashish DK, Verma SK (2021) Robustness of self-compacting concrete containing waste foundry sand and metakaolin: A sustainable approach. J Hazard Mater 401:123329. https://doi.org/10.1016/j.jhazmat.2020.123329
2. Sharma R (2021) Effect of wastes and admixtures on compressive strength of concrete. JEDT 19:219–244. https://doi.org/10.1108/JEDT-01-2020-0031
3. Bożym M, Klojzy-Karczmarczyk B (2021) Assessment of the mercury contamination of landfilled and recovered foundry waste – a case study. Open Chem 19:462–470. https://doi.org/10.1515/chem-2021-0043
4. Kumar Sinha N, Kumar J, Choudhary IN (2021) Utilization of industrial solid waste as a mold material in the foundry industry. Mater Today: Proceedings 46:1492–1498. https://doi.org/10.1016/j.matpr.2020.11.748
5. Sushma D, Richa S (2015) Use of nanoparticles in water treatment: a review. Int Res J Environ Sci 4:103–106
6. Salahshoor Z, Shahbazi A (2014) Review of the use of mesoporous silicas for removing dye from textile wastewater. Eur J Environ Sci 4:116–130. https://doi.org/10.14712/23361964.2014.7
7. Bader AT, Aljeboree AM, Alkaim AF (2019) Removal of methyl violet (MV) from aqueous solutions by adsorption using activated carbon from pine husks (plant waste source). Plant Archives 19:898–901
8. Adegoke KA, Bello OS (2015) Dye sequestration using agricultural wastes as adsorbents. Water Resources and Industry 12:8–24. https://doi.org/10.1016/j.wri.2015.09.002
9. Zhao Y, Yang H, Sun J (2021) Enhanced Adsorption of Rhodamine B on Modified Oil-Based Drill Cutting Ash: Characterization, Adsorption Kinetics, and Adsorption Isotherm. ACS Omega 6:17086–17094. https://doi.org/10.1021/acsomega.1c02214
10. Alswieleh AM, Albahar HY, Alfawaz AM (2021) Evaluation of the Adsorption Efficiency of Glycine-, Iminodiacetic Acid -, and Amino Propyl-Functionalized Silica Nanoparticles for the Removal of Potentially Toxic Elements from Contaminated Water Solution. J Nanomater 2021:1–12. https://doi.org/10.1155/2021/6664252
11. Putz A-M, Ciopec M, Negrea A (2021) Comparison of Structure and Adsorption Properties of Mesoporous Silica Functionalized with Aminopropyl Groups by the Co-Condensation and the Post Grafting Methods. Materials 14:628. https://doi.org/10.3390/ma14030628
12. Chakraborty R, Asthana A, Singh AK (2022) Adsorption of heavy metal ions by various low-cost adsorbents: a review. Int J Environ Anal Chem 102:342–379. https://doi.org/10.1080/03067319.2020.1722811
13. Yang Z, Yang H, Jiang Z (2013) Flocculation of both anionic and cationic dyes in aqueous solutions by the amphoteric grafting flocculant carboxymethyl chitosan-graft-polyacrylamide. J Hazard Mater 254–255:36–45. https://doi.org/10.1016/j.jhazmat.2013.03.053
14. Bassyouni DG, Hamad HA, El-Ashtoukhy E-SZ (2017) Comparative performance of anodic oxidation and electrocoagulation as clean processes for electrocatalytic degradation of diazo dye Acid Brown 14 in aqueous medium. J Hazard Mater 335:178–187. https://doi.org/10.1016/j.jhazmat.2017.04.045
15. Golder AK, Samanta AN, Ray S (2006) Anionic reactive dye removal from aqueous solution using a new adsorbent—Sludge generated in removal of heavy metal by electrocoagulation. Chem Eng J 122:107–115. https://doi.org/10.1016/j.cej.2006.06.003
16. Xin S, Yang N, Gao F (2017) Three-dimensional polypyrrole-derived carbon nanotube framework for dye adsorption and electrochemical supercapacitor. Appl Surf Sci 414:218–223. https://doi.org/10.1016/j.apsusc.2017.04.109
17. Sun W, Zhang C, Chen J (2017) Accelerating biodegradation of a monoazo dye Acid Orange 7 by using its endogenous electron donors. J Hazard Mater 324:739–743. https://doi.org/10.1016/j.jhazmat.2016.11.052
18. Ali H (2010) Biodegradation of synthetic dyes—a review. Water Air Soil Pollut 213:251–273. https://doi.org/10.1007/s11270-010-0382-4
19. Guettaï N, Ait Amar H (2005) Photocatalytic oxidation of methyl orange in presence of titanium dioxide in aqueous suspension Part I: Parametric study. Desalination 185:427–437. https://doi.org/10.1016/j.desal.2005.04.048
20. Bm V, M V (2015) Photocatalytic Degradation of Toxic Methyl Red Dye Using Silica Nanoparticles Synthesized from Rice Husk Ash. J Environ Anal Toxicol 05: https://doi.org/10.4172/2161-0525.1000336
21. Castanheira B, Otubo L, Oliveira CLP (2022) Functionalized mesoporous silicas SBA-15 for heterogeneous photocatalysis towards CECs removal from secondary urban wastewater. Chemosphere 287:132023. https://doi.org/10.1016/j.chemosphere.2021.132023
22. Lum PT, Foo KY, Zakaria NA, Palaniandy P (2020) Ash based nanocomposites for photocatalytic degradation of textile dye pollutants: a review. Mater Chem Physics 241:122405. https://doi.org/10.1016/j.matchemphys.2019.122405
23. Yang H, Teng F, Gu W (2017) A simple post-synthesis conversion approach to Zn(OH)F and the effects of fluorine and hydroxyl on the photodegradation properties of dye wastewater. J Hazard Mater 333:250–258. https://doi.org/10.1016/j.jhazmat.2017.03.039
24. Abu Rumman G, Al-Musawi TJ, Sillanpaa M, Balarak D (2021) Adsorption performance of an amine-functionalized MCM–41 mesoporous silica nanoparticle system for ciprofloxacin removal. Environ Nanotechnol Monit Manag 16:100536. https://doi.org/10.1016/j.enmm.2021.100536
25. Mallik AK, Moktadir MdA, Rahman MdA et al (2022) Progress in surface-modified silicas for Cr(VI) adsorption: a review. J Hazard Mater 423:127041. https://doi.org/10.1016/j.jhazmat.2021.127041
26. Abshirini Y, Foroutan R, Esmaeili H (2019) Cr(VI) removal from aqueous solution using activated carbon prepared from *Ziziphus-spina christi* leaf. Mater Res Express 6:045607. https://doi.org/10.1088/2053-1591/aafb45
27. Patil SA, Suryawanshi UP, Harale NS (2020) Adsorption of toxic Pb(II) on activated carbon derived from agriculture waste (Mahogany fruit shell): isotherm, kinetic and thermodynamic study. Int J Environ Anal Chem 1–17. https://doi.org/10.1080/03067319.2020.1849648
28. Manyangadze M, Chikuruwo NHM, Narsaiah TB (2020) Enhancing adsorption capacity of nano-adsorbents via surface modification: A review. S Afr J Chem Eng 31:25–32. https://doi.org/10.1016/j.sajce.2019.11.003
29. Yagub MT, Sen TK, Afroze S, Ang HM (2014) Dye and its removal from aqueous solution by adsorption: A review. Adv Coll Interface Sci 209:172–184. https://doi.org/10.1016/j.cis.2014.04.002
30. Imran M, Shaharoona B, Crowley DE (2015) The stability of textile azo dyes in soil and their impact on microbial phospholipid fatty acid profiles. Ecotoxicol Environ Saf 120:163–168. https://doi.org/10.1016/j.ecoenv.2015.06.004
31. Wang Z, Xue M, Huang K, Liu Z (2011) Textile Dyeing Wastewater Treatment. In: Hauser P (ed) Advances in Treating Textile Effluent. InTech

32. Singh K, Arora S (2011) Removal of Synthetic Textile Dyes From Wastewaters: A Critical Review on Present Treatment Technologies. Crit Rev Environ Sci Technol 41:807–878. https://doi.org/10.1080/10643380903218376
33. Rodríguez-Couto S, Osma JF, Toca-Herrera JL (2009) Removal of synthetic dyes by an eco-friendly strategy. Eng Life Sci 9:116–123. https://doi.org/10.1002/elsc.200800088
34. Krishnan S, Chatterjee S, Solanki A (2020) Aminotetrazole-Functionalized SiO_2 Coated MgO Nanoparticle Composites for Removal of Acid Fuchsin Dye and Detection of Heavy Metal Ions. ACS Appl Nano Mater 3:11203–11216. https://doi.org/10.1021/acsanm.0c02351
35. Patil SA, Patil SK, Sartape AS (2020) A *Pongamia pinnata* pods based activated carbon as an efficient scavenger for adsorption of toxic Co(II): kinetic and thermodynamic study. Sep Sci Technol 55:2904–2918. https://doi.org/10.1080/01496395.2019.1659366
36. Hymavathi D, Prabhakar G (2017) Optimization, equilibrium, and kinetic studies of adsorptive removal of cobalt(II) from aqueous solutions using *Cocos nucifera* L. Chem Eng Commun 204:1094–1104. https://doi.org/10.1080/00986445.2017.1338570
37. Ruiz-Cañas MC, Corredor LM, Quintero HI (2020) Morphological and Structural Properties of Amino-Functionalized Fumed Nanosilica and Its Comparison with Nanoparticles Obtained by Modified Stöber Method. Molecules 25:2868. https://doi.org/10.3390/molecules25122868
38. Durairaj K, Senthilkumar P, Velmurugan P (2019) Sol-gel mediated synthesis of silica nanoparticle from Bambusa vulgaris leaves and its environmental applications: kinetics and isotherms studies. J Sol-Gel Sci Technol 90:653–664. https://doi.org/10.1007/s10971-019-04922-7
39. Shafqat SS, Khan AA, Zafar MN (2019) Development of amino-functionalized silica nanoparticles for efficient and rapid removal of COD from pre-treated palm oil effluent. J Market Res 8:385–395. https://doi.org/10.1016/j.jmrt.2018.03.002
40. Vejayakumaran P, Rahman IA, Sipaut CS (2008) Structural and thermal characterizations of silica nanoparticles grafted with pendant maleimide and epoxide groups. J Colloid Interface Sci 328:81–91. https://doi.org/10.1016/j.jcis.2008.08.054
41. Noushad M, Ab Rahman I, Husein A, Mohamad D (2016) Nano-hybrid dental composite using silica from biomass waste. Powder Technol 299:19–25. https://doi.org/10.1016/j.powtec.2016.05.035
42. Raj SI, Jaiswal A, Uddin I (2019) Tunable porous silica nanoparticles as a universal dye adsorbent. RSC Adv 9:11212–11219. https://doi.org/10.1039/C8RA10428J
43. Mahmoodi NM, Khorramfar S, Najafi F (2011) Amine-functionalized silica nanoparticle: Preparation, characterization and anionic dye removal ability. Desalination 279:61–68. https://doi.org/10.1016/j.desal.2011.05.059
44. Barma MD, Kannan SD, Indiran MA (2020) Antibacterial Activity of Mouthwash Incorporated with silica nanoparticles against S. aureus, S. mutans, E. faecalis: An in-vitro study. J Pharm Res Int 25–33. https://doi.org/10.9734/jpri/2020/v32i1630646
45. Ghorai S, Sinhamahpatra A, Sarkar A (2012) Novel biodegradable nanocomposite based on XG-g-PAM/SiO2: Application of an efficient adsorbent for Pb2+ ions from aqueous solution. Biores Technol 119:181–190. https://doi.org/10.1016/j.biortech.2012.05.063
46. Langmuir I (1916) The constitution and fundamental properties of solids and liquids. part I. solids. J Am Chem Soc 38:2221–2295. https://doi.org/10.1021/ja02268a002